

LUCES-MV: A Multi-View Dataset for Near-Field Point Light Source Photometric Stereo

Fotios Logothetis
Toshiba Europe
Cambridge UK
fotios.logothetis
@toshiba.eu

Ignas Budvytis
Independent researcher
Cambridge UK
ignas.budvytis
@gmail.com

Stephan, Liwicki
Toshiba Europe
Cambridge UK
stephan.liwicki
@toshiba.eu

Roberto Cipolla
University of Cambridge
Cambridge UK
rc10001@cam.ac.uk

Abstract

The biggest improvements in Photometric Stereo (PS) field has recently come from adoption of differentiable volumetric rendering techniques such as NeRF or Neural SDF achieving impressive reconstruction error of 0.2mm on DiLiGenT-MV benchmark. However, while there are sizeable datasets for environment lit objects such as Digital Twin Catalogue (DTS), there are only several small Photometric Stereo datasets which often lack challenging objects (simple, smooth, untextured) and practical, small form factor (near-field) light setup.

To address this, we propose LUCES-MV, the first real-world, multi-view dataset designed for near-field point light source photometric stereo. Our dataset includes 15 objects with diverse materials, each imaged under varying light conditions from an array of 15 LEDs positioned 30 to 40 centimeters from the camera center. To facilitate transparent end-to-end evaluation, our dataset provides not only ground truth normals and ground truth object meshes and poses but also light and camera calibration images.

We evaluate state-of-the-art near-field photometric stereo algorithms, highlighting their strengths and limitations across different material and shape complexities. LUCES-MV dataset offers an important benchmark for developing more robust, accurate and scalable real-world Photometric Stereo based 3D reconstruction methods.

1. Introduction

The quality of object shape reconstruction has improved rapidly over recent years. Major milestones include the adoption of neural shape representations such as NeRF [40] and DeepSDF [44] and subsequent structure in differentiable rendering process (e.g. Ref-NeRF [51], NeILF++ [61], NERO [29]). While improving neural re-

rendering accuracy is believed to also improve the accuracy of the recovered shape, it is most often not evaluated. In fact, in practice we see a significant discrepancy between state-of-the-art neural rendering methods and photometric stereo methods targeted explicitly at shape reconstruction as illustrated in Figure 2 (to be contrasted with Figure 5).

In the Photometric Stereo community, shape reconstruction first utilized naïve volumetric rendering [21], and evolved to leverage normals as a loss for shape estimation [6, 57]. Most recently both the rendering and normals signals, are employed for relatively accurate shape reconstruction [4, 31]. The true impact of this evolution, however, is hidden by evaluations on the saturated DiLiGenT-MV [25] (as shown by [31]), which is almost always the only benchmark used. We note, there is a clear need for new data, given the significant progress and promise of photometric stereo as powerful approach to shape reconstruction.

To alleviate this problem, we propose our LUCES-MV dataset, an extension of LUCES [37]. Our dataset contains 10 objects¹ of varying materials and diverse shapes. Compared to DiLiGenT-MV [25] we improve in several aspects:

- We capture high resolution (2080×1552 vs 612×512) images under true near-field lighting conditions (objects are within 30-40cm).
- We provide stereo pairs for all views to foster the improvement binocular photometric stereo methods [30].
- We add a challenging metal object (*Cup*) as well as objects with highly complex shapes such as *House* or

¹In fact we provide Photometric Stereo images from 36 viewpoints of which 6 are provided with accurate ground truth pose and ground truth meshes for 15 objects from original LUCES [37] benchmark. However, due to rotational symmetry, we do not include pose alignments or shape reconstruction accuracies for 4 objects: *Ball*, *Bell*, *Jar*, *Tool* and we also add one more transparent object - *Glass*. We hope future unposed Photometric Stereo methods to be able to tackle such data. See more information about those objects in the supplementary material.

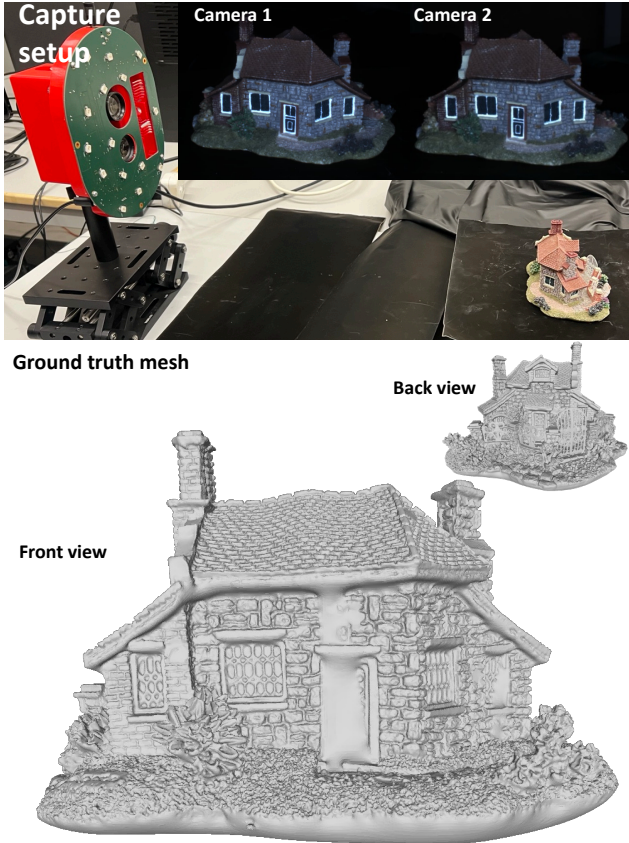


Figure 1. This figure illustrates our capture setup (top half). Capture device is enclosed by the red casing which houses a 15 LED lights and two RGB cameras. The object (a miniature *House* in this case) is placed on a bluetooth controllable turntable covered by non-reflective material on the right. The average images from 15 lights of a particular view is shown on the top right corner. The ground truth mesh of the object scan is illustrated on the bottom of the figure. The shape of the *House* is far more complex than the shape of any object in current Photometric Stereo datasets such as DiLiGenT-MV [25]. See examples of other challenging objects in Figure 3.

concave *Bowl* (see Figure 3).

- We provide all captured images in its raw format (to encourage PS methods to avoid using demosaiced images affected by processing artifacts) and also provide light and camera calibration images so that complete recalibration can be performed, if required (common complaint [31] with DiLiGenT-MV [25] benchmark).

Our contributions are as follows: (a) we introduce a novel near-field multi-view PS dataset of 10 posed and 5 unposed objects (b) evaluate key SOTA algorithms for single view, binocular and multi-view Photometric Stereo, (c) identify the future challenges for the PS research. The dataset and the evaluation of the methods is publicly avail-

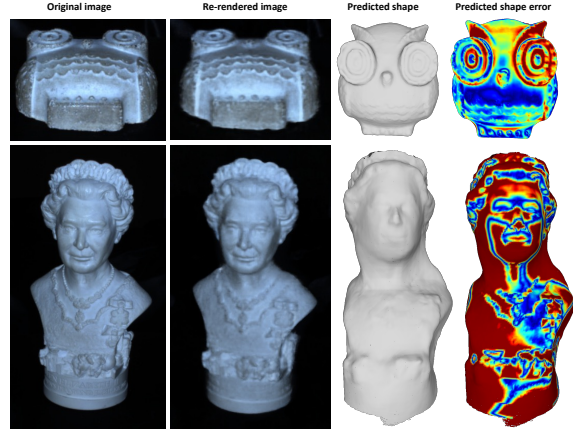


Figure 2. In this figure we show a reconstruction result of Neuralangelo [27] using 36 pairs (average images of 15 light images are used) of stereo views. Note that the re-rendered images match the original very well (PSNR of 32.8 and 38.8 for *Owl* and *Queen* respectively). However, the predicted shape is significantly worse for *Queen* (1.68mm) than for *Owl* (0.44mm). This should be compared to results of RNb-NeuS [5] (*Owl* - 0.37mm, *Queen* - 0.21mm), also shown qualitatively in Figure 5.

able².

The rest of this paper is structured as follows. Section 2 discusses the key approaches and datasets used in Photometric Stereo community. Section 3 describes our data capture process. Whereas Sections 4 and 5 describes the experiments performed and results obtained respectively.

2. Related Work

In this section we review key single view and multi-view photometric stereo, neural surface reconstruction methods and datasets.

Single view photometric stereo. Early PS approaches [1, 7, 36, 52, 55] have employed classical optimizations for obtaining 2D normal maps and thus their applicability has been limited in objects of mostly diffuse reflection. More recently, deep learning-based approaches such as [14, 18, 32] for the far-field problem and [12, 33, 48] for the near field, have significantly improved the single view normal estimation accuracy. Additionally, large synthetic datasets in conjunction with transformer models also allow tackling the weakly uncalibrated setting in works like [8, 23, 24, 58]. Finally, [15] introduced the universal PS concept with further improvements in [16] and [13].

Multi-view photometric stereo. Obtaining accurate shape from a single view has been challenging as well as ill-posed in many cases. Multiview PS methods have traditionally been employed to solve this issue by using infor-

²<https://drive.google.com/drive/folders/1634yweYUpLvNPC1qEG8hRpmhtxVtFrLi?usp=sharing>



Figure 3. The top part of figure shows iPhone images of 10 objects (first two rows) in the LUCES-MV dataset for which not only the photometric stereo images and ground truth meshes but also ground truth poses for 12 frames (6 pairs of stereo images) are provided. The final 5 objects (row 3) has all information except the alignment between images and ground truth meshes. We hope that future methods of unposed or weakly posed Photometric Stereo will be able to tackle the estimation and evaluation of the shape of these objects.

mation from multiple view and multiple lights. Classical MVPS approaches applicable on diffuse reflectance objects include [35, 42, 43, 63] and [25] which is applicable to general materials.

Neural surfaces. Just like in the single view case, the introduction of deep methods, especially through the use of neural surfaces have revolutionized the multi-view reconstruction problem. The first seminal works are NeRF [40], IDR [60], VolSDF [59] and NeuS [54] More recent methods that have advanced the sophistication of the neural rendering pipeline include Ref-NeRF [51], NERO [29] and NeILF++ [61] and Neuralangelo [27] which has shown impressive reconstruction quality on large MV datasets.

The first Neural MVPS works [19–21, 57, 62] have used 2D feature (normals, albedo) rendering in order to maximize consistency with the output of single-view PS methods. These has been the case even for the most recent methods including Supernormal [6], which renders patches of normals and RNb-NeuS [5] which uses normal and albedo maps to render virtual diffuse images.

Very few methods have attempted to re-render the original PS images including the binocular photometric stereo method [30], Brahimi et. al [4] and the most recent NPLMV-PS [31]. We speculate that the lack of availability

of calibrated MVPS data is responsible and that LUCES-MV dataset will push the research frontier forward.

Photometric Stereo datasets. PS real datasets have been very limited for a long time with early methods including synthetic data evaluations and only qualitative real [34, 38]. Some early works including some real data include [2], [56] and [46] however non of these data are extensive enough to be considered a trusted benchmark. Some early synthetic datasets include SculpturePS [48], CyclePS [14] and BlobbyPS [9].

The first widely used PS dataset of significant scale is DiLiGenT [50] containing 10 objects light from 96 approximately directional lights. Although the image resolution was limited to 612×512 px, DiLiGenT has been the gold standard benchmark for single view PS since. Further extension have significantly improved the single view PS data availability adding a lot more materials in [47], high accuracy planar objects [53] and translucency [11]. In addition, DiLiGenT-MV [25] is the only multi-view extension that however only contains 5 objects in the original 612×512 low resolution. One limitation of the DiLiGenT* datasets is that they are all in a far-field setting, containing approximate orthographic cameras and approximate directional lights. This minimizes the potential of evaluation near field meth-

ods. To mitigate this issue, the LUCES [37] and LUCES-stereo [30] datasets were introduced containing near cameras and point light sources. This work extends Lucas* to the MVPS setting.

Finally, note that there are extensive multi-view stereo datasets such as DTU [17], Tanks and Temples and [22] and DTC [3] by Meta, however, the last of controlled and varied illumination on these datasets makes PS reconstruction impossible.

3. Data Capture

This section gives an overview of the calibration procedure, data capture as well as ground truth capture procedure. It also provides an overview of the contents of the dataset.

3.1. Photometric Stereo Data Capture

The Photometric Stereo setup. Our photometric capture setup (see Figure 1) consists of a stereo pair of Flea3 FL3-U3-32S2C-CS 1/2.8" Color USB 3.0 pointgray cameras (resolution 2080×1552 px, mounting 8mm lenses) rigidly attached to a custom circuit board containing 15 Golden Dragon OSRAM LEDs. The approximate dimensions of the circuit board are $14\text{cm} \times 18\text{cm}$ with the camera baseline being 4.5cm. Objects are positioned on a computer controlled turntable around 40cm away from the capture device. Black absorbing material is used on the surface of the turntable and around the setup in order to minimise the effect of interreflections. The whole setup is completely automatic and allows repeatable capture of any object (with the turntable rotation accuracy of around 0.1°). Black, polyurethane-coated nylon fabric is used to cover the background.

Camera focus, aperture and exposure were kept constant to make sure the calibration was consistent for the whole dataset. In particular, the aperture was set to the minimum to best approximate a pinhole, and no analogue gain with long exposure (0.6s) was used to minimise the effect of camera noise. All other camera preprocessing (white-balance etc) was also turned off. In addition, to further improve signal to noise ratio (as the maximum precision of the cameras is 10bits per pixel), for each light, 4 raw images were captured. In addition, even though the setup was in a completely dark room, for each view, an ‘ambient’ image was also captured as this is used to calibrate the zero level of each camera pixel.

All raw data including calibration have been saved and will be made available.

3.2. Calibration

Camera Intrinsic. Calibration pattern from <https://calib.io/> is used to create checkerboard images. The intrinsic are estimated using the OpenCV calibration toolbox. 7 views of the checkerboard, 60 rotations each are

captured giving a total of 420 checkerboard images. The calibration re-projection error of 0.2px is obtained. Images are wrapped to compensate ration distortion, place camera center in middle of image and equalize focal lengths.

Point Light Calibration. The standard approach to point light source Photometric Stereo ([39, 45]) is employed. An anisotropic angular dissipation as well as inverse square distance attenuation is assumed. Thus if the light source position and orientation are \mathbf{P} and $\hat{\mathbf{D}}$ respectively, the lighting vector \mathbf{L} of a world point \mathbf{X} is computed as $\mathbf{L} = \mathbf{P} - \mathbf{X}$. For an angular dissipation factor μ , the angular dissipation is $(\hat{\mathbf{L}} \cdot \hat{\mathbf{D}})^\mu$, where $\hat{\mathbf{L}} = \frac{\mathbf{L}}{\|\mathbf{L}\|}$ is the normalized lighting vector. Combining the above quantities with an intrinsic brightness Φ and the inverse distance factor $1/\|\mathbf{L}\|^2$, gives the overall point attenuation (of the 3D world point \mathbf{X}) as:

$$a(\mathbf{X}) = \Phi \frac{(\hat{\mathbf{L}} \cdot \hat{\mathbf{D}})^\mu}{\|\mathbf{L}\|^2}. \quad (1)$$

The estimation of parameters (\mathbf{P} , $\hat{\mathbf{D}}$, μ , Φ) of Equation 1 is achieved using captures of diffuse reflectance calibration target (see supplementary material). Indeed, images of the target should satisfy a diffuse irradiance equation:

$$\mathbf{I} = \Phi \rho \hat{\mathbf{L}} \cdot \hat{\mathbf{N}}. \quad (2)$$

with $\rho = 0.99$ being the albedo according to the material data-sheet. Surface normal $\hat{\mathbf{N}}$ and 3D position of the planar target is easily estimated by performing manual segmentation to find the edges (and subsequently the corners) of the planar pattern followed by PnP-based pose estimation. Simple differentiable rendering (using Keras of Tensorflow v2.0) Equation 2 allows recovery of all calibration parameters in a similar manner as in [37]. 13 stereo pair views (total 26 views x 15 lights) images are used achieving re-rendering error of 0.01.

3.3. 3D Ground Truth Capture

We are re-using the ground truth scans from the original LUCES [37] dataset with an additional object: *Glass*. These were made with 2 scanners. Ground truth meshes for *Bowl*, *Buddha*, *House*, *Owl*, *Queen* were obtained with optical GOM ATOS Core 80/135 3D scanner (reported accuracy of 0.03mm). No spray coating or markers have been used to ease the acquisition to keep the geometry of the object consistent with the PS data. The remain objects: *Ball*, *Bell*, *Bunny*, *Cup*, *Die*, *Glass*, *Hippo*, *Jar*, *Tool*, *Squirrel* with the Zeiss CT scanner M1500/225 kV which provides an accuracy within the order of $9\mu\text{m}$.

Alignment. We use the standard 2D to 3D alignment procedure as in [37, 50]. This involves the mutual information filter of MeshLab [10] with manual initialization and then

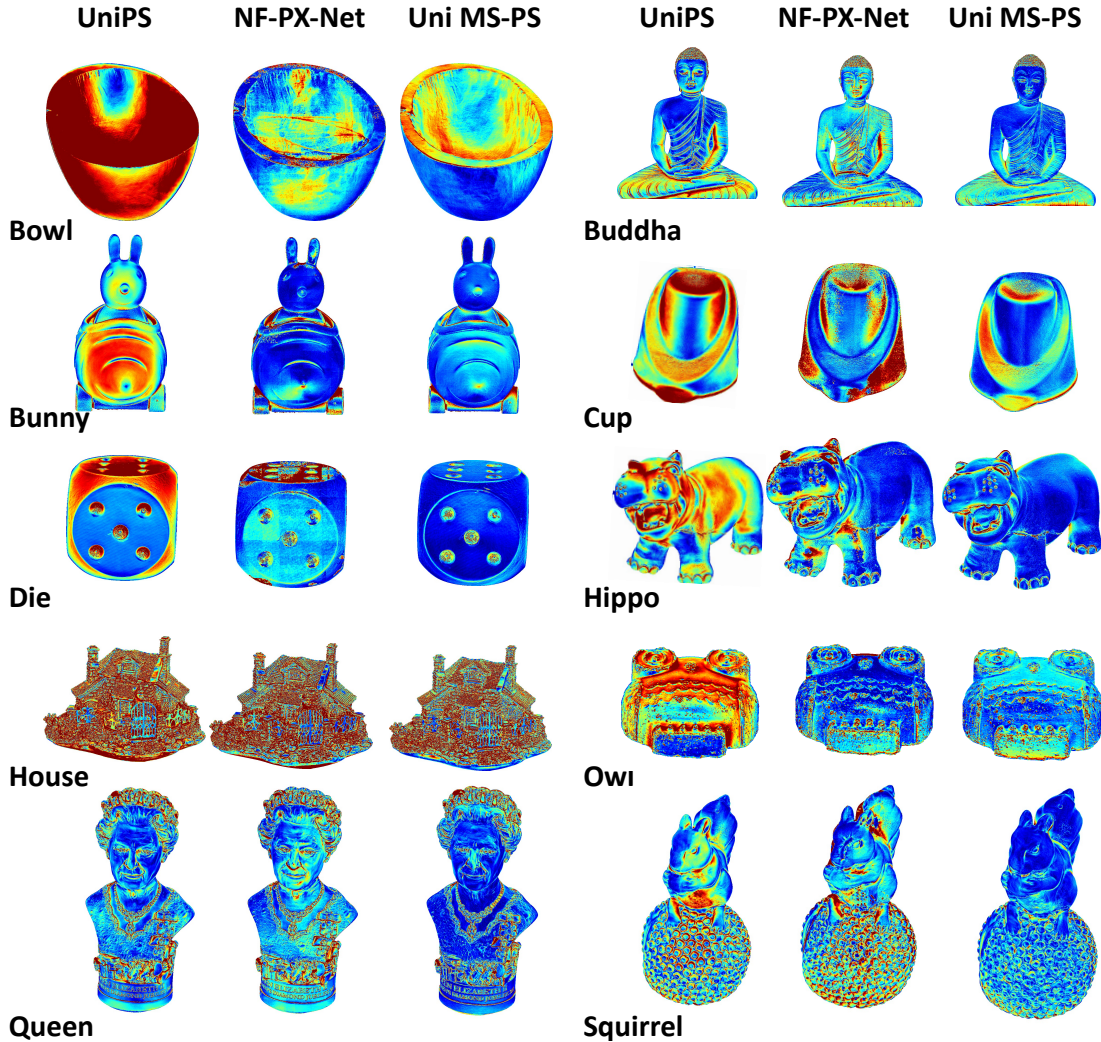


Figure 4. This figure shows normal error map predictions for three normal estimation methods. Uni MS-PS [13] significantly outperforms other methods. See corresponding quantitative results in Table 1. Dark red color corresponds to an angular error of 15 degrees and dark blue - to zero.

repetitive refinement (until ‘pixel perfect’ using the semi-transparent overlay). For 2D reference image, the average photometric stereo image was used, with additional manual image processing (exposure, brightness and contrast). Using the aligned meshes, ground truth normal maps and segmentation masks were rendered (with PyTorch3D).

3.4. Dataset Overview

LUCES-MV contains 10 pose aligned objects namely *Bowl*, *Buddha*, *Bunny*, *Cup*, *Die*, *Hippo*, *House*, *Owl*, *Queen*, *Squirrel* as well as 5 unaligned (due to rotational symmetry) objects *Ball*, *Bell*, *Glass*, *Jar*, *Tool* of diverse materials and geometry as shown in Figure 3. Noteworthy properties are extreme concavity (creating shadows and self reflections) in *Bowl*, extreme metallic shininess in *Cup* ex-

treme complicated topology in *House*. See a more in depth explanation in the supplementary material.

For each object, PS images were captured at every 10° leading to a total of 36 stereo pairs, (72 views x 15 PS images = 1080 RGB images per object). However, due to the manual aligning processes being laborious, for each object only 12 views were aligned (all stereo pairs every 60°) and that constitutes the main part of the dataset which is used for evaluation experiments of Section 4. Nevertheless, all of the data will be released (including all 4 Bayer RAW images that are used to generate each RGB image), inviting the community to improve calibration-free methods; standard SFM like COLMAP [49] and self-calibrating neural reconstruction like BARF [28] are unreliable on texture-less object on completely black background.

Method	Error	Bowl	Buddha	Bunny	Cup	Die	Hippo	House	Owl	Queen	Squirrel	Average
UniPS [16] (uncalibrated)	MAE	37.3	18.3	15.5	23.9	25.3	18.9	37.6	28.2	17.7	17.0	24.0
Uni MS-PS [13] (uncalibrated)	MAE	17.5	13.7	10.6	12.3	10.3	9.6	33.0	14.7	12.9	11.3	14.6
NF-PX-Net [33] (calibrated)	MAE	16.7	20.1	12.8	19.9	19.4	14.3	36.2	18.8	15.8	19.7	19.4

Table 1. This figure provides the evaluation of two uncalibrated PS normal estimation methods (UniPS [16] and Uni MS-PS [13]) and one calibrated normal estimation method NF-PX-Net [33]. Uni MS-PS [13] being the most recent method outperforms other competitors on all objects except Bowl. Note, however the average angular error of 14.6° indicating a large room for improvement especially for objects like *Bowl*, *House*, *Cup* and *Buddha*.

4. Experiment setup

We evaluated multiple different methods on three key Photometric stereo tasks: single view normal estimation, binocular photometric stereo shape estimation and multi-view photometric stereo shape estimation which have different classes of applications

Single view normal estimation. For single view normal estimation we compare two SOTA universal photometric stereo methods UniPS [16] and Uni MS-PS [13] as well as a calibrated normal estimation method NF-PX-Net [33]. These 3 methods are among the current best performers on single view DiLiGenT [50] and have public test code and network weights. UniPS [16] also provides an estimate of albedo maps. For all methods, ground truth segmentation maps are provided. NF-PX-Net [33] requires light calibration parameters are well as an approximate mean depth.

We evaluate mean angular error (as it is the standard in single view PS datasets like [50]) shown in Table 1, obtained by taking an average pixel wise error for all 12 images per object. We also provide a visualization of pixelwise angular error for initial pose, viewpoint 1 for all methods and all objects in Figure 4.

Binocular photometric stereo. We also evaluate modern binocular photometric stereo method of [30]. Quantitatively we evaluate mean and median shape errors computed as bidirectional Hausdorff distance (using the python interface of MeshLab [10]) between all *visible* points on ground truth and predicted meshes. Quantitative in Table 2 and qualitative results are provided in supplementary. Note that qualitative visualization shows the shape error from reconstruction to ground truth for all points, but only visible points are included on the computation in Table 2.

Multi-view photometric stereo. The key experiments involve evaluating SOTA multi-view photometric stereo methods of Supernormal [6], RNb-NeuS [5] and NPLMV-PS [31]. As the the latter method has versions which either uses only normal information (N) or only pixel intensities information (I) we provide three evaluation settings, including where both pieces of information are used. The same evaluation (Table 2) and visualization (Figure 5) metrics are used as for binocular photometric stereo method [30].

Note we use Uni MS-PS [13] normals for all three methods and the albedo maps of UniPS [16] for RNb-NeuS [5]. We note that normal only (N) version of NPLMV-PS [31] is conceptually very similar to Supernormal [6] and intensities only (I) version of NPLMV-PS [31] is conceptually very similar to [4], which unfortunately is closed source.

5. Results

We discuss the result of three types of experiments:

Single view normal estimation. We observe that UniPS [16] has significantly worse performance than other two methods. This is not very surprising as it was optimized for far-field Photometric Stereo and thus cannot directly cope with near-light attenuation and perspective distortion. Uni MS-PS [13] shows best performance (both quantitatively and qualitatively) on all objects except *Bowl*, despite NF-PX-Net [32] benefiting from a calibrated normal estimation network. Specifically, NF-PX-Net [33] has slightly poorer performance than uncalibrated Uni MS-PS [13] as it includes less material augmentation of its training dataset (e.g. see a very good performance of NF-PX-Net [32] on *Queen* object) and also, since it has been trained on independent samples of observational maps it has inferior ability to correctly predict normals along the edges and in regions suffering from severe reflections). Finally, NF-PX-Net [33] also shows significantly poor ability to predict normals at oblique angles but is competitive to Uni MS-PS [13] on smooth regions (e.g. *Bunny*, body of *Hippo*, face of *Squirrel*). Poor performance on *Bowl*, *House*, *Cup* of Uni MS-PS [13] hints that significant research efforts are required to better material modeling for single view Photometric Stereo, which we hope our dataset will contribute to fostering.

Binocular photometric stereo. While binocular photometric stereo [30] has many applications in robotics, there are yet to appear a significant number of competing methods. Binocular PS result of [30] (first section in Table 2) is significantly worse than the respective multi-view results, as well as the original result that it was obtained in LUCES-ST [30] and 2 views on DiLiGenT-MV [25]. The qualitative visualization (in supplementary) reveals that although

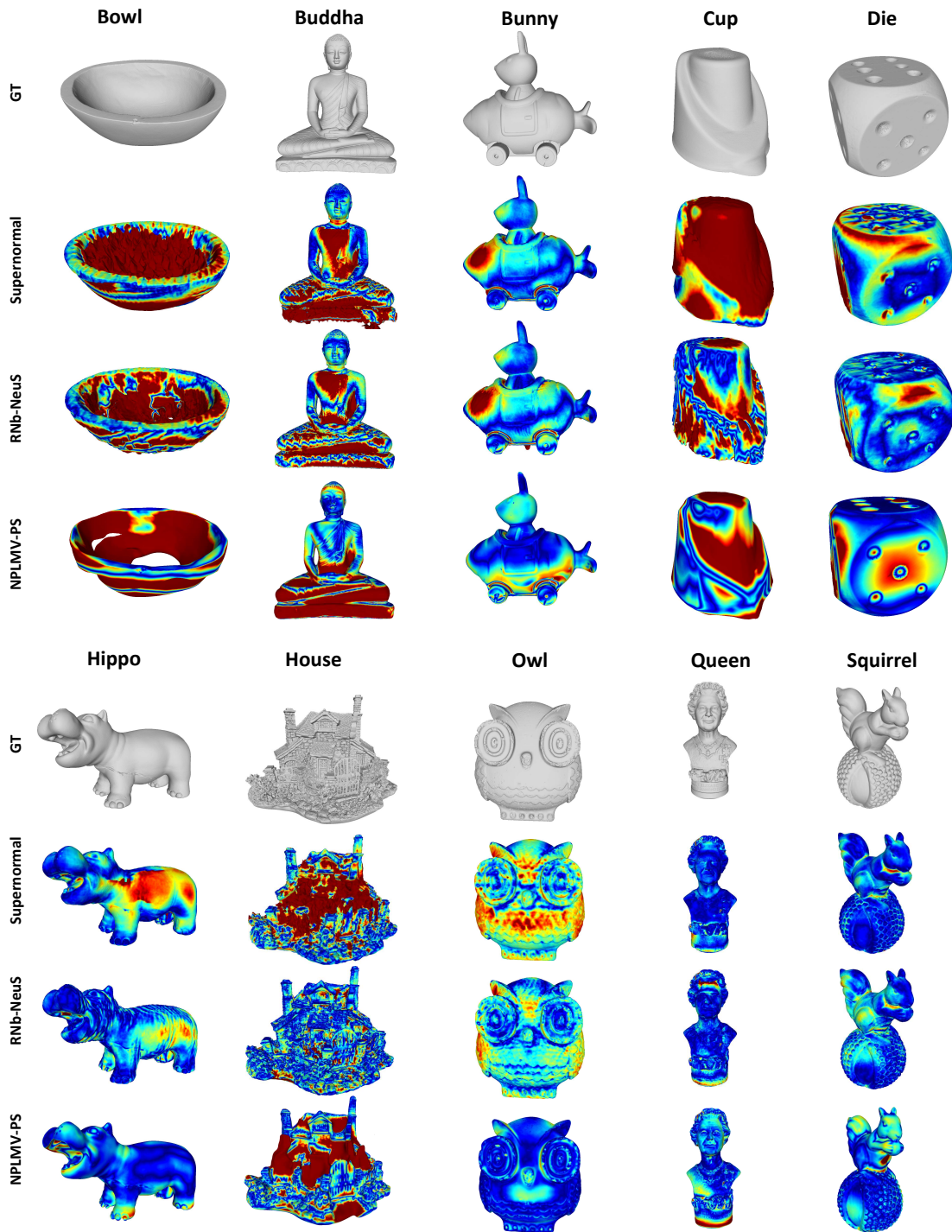


Figure 5. This figure illustrates reconstruction to GT Hausdorff distance for each point of predicted meshes for all three MVPS methods. We emphasize that although the distance for all points is visualized, the numbers reported on Table 2 are computed on visible points only (computing visibility for both GT and reconstructions). As indicated by Table 2, RNb-NeuS [5] shows same or slightly better performance than other two methods. In particular, significantly lower error on *House* object is very impressive and is likely due to implicit stereo matching of the texture through the use of albedo maps. As evident from the results shape error could be significantly improved on most of the objects. Improvements in both better normal estimation as well as neural rendering of pixel intensities are required to improve SOTA on LUCES-MV dataset. Dark red color corresponds to per point closest distance of 1 millimeter and dark blue - 0.

Method	Error	Bowl	Buddha	Bunny	Cup	Die	Hippo	House	Owl	Queen	Squirrel	Average
Binocular-PS [30]	MN	19.02	5.67	1.93	5.37	2.97	10.12	5.50	1.72	2.60	3.67	5.86
	MD	18.68	4.54	1.78	5.39	2.84	9.19	5.00	0.81	2.54	1.60	5.24
RNb-NeuS [5] (GT-N)	MN	0.17	0.17	0.07	0.51	0.07	0.10	0.13	0.03	0.04	0.04	0.13
	MD	0.09	0.05	0.04	0.27	0.07	0.08	0.04	0.03	0.03	0.03	0.07
RNb-NeuS- [5]	MN	1.37	0.68	0.39	1.10	0.41	0.28	0.47	0.37	0.21	0.26	0.55
	MD	0.81	0.45	0.27	0.80	0.28	0.22	0.31	0.34	0.16	0.23	0.39
Supernormal [6]	MN	4.04	1.08	0.41	1.41	0.61	0.35	1.26	0.48	0.22	0.22	1.01
	MD	2.69	0.87	0.33	1.32	0.52	0.32	0.92	0.46	0.20	0.20	0.78
NPLMV-PS [31] (N)	MN	2.14	1.06	0.50	1.22	0.79	0.28	1.66	0.26	0.33	0.22	0.85
	MD	1.81	0.63	0.33	0.98	0.51	0.23	0.67	0.19	0.24	0.17	0.57
NPLMV-PS [31] (I)	MN	4.43	1.27	0.42	1.56	0.53	1.61	1.36	0.27	0.50	0.47	1.24
	MD	2.56	0.79	0.27	1.19	0.49	1.10	0.71	0.21	0.41	0.42	0.82
NPLMV-PS [31] (N+I)	MN	2.03	0.91	0.45	1.22	0.43	0.25	1.06	0.25	0.33	0.24	0.72
	MD	1.59	0.55	0.32	0.98	0.32	0.26	0.51	0.18	0.28	0.19	0.52

Table 2. This table shows the computed results for a binocular photometric stereo method of [30] and three SOTA multi-view photometric stereo methods. RNb-NeuS [5] achieves the best mean shape error of 0.55mm and significantly (by 0.1mm or more) outperforms all of the competing approaches except for *Hippo*, *Owl* and *Squirrel*. Unlike in DiLiGenT-MV [25] benchmark, as reported by [31] the error ratio (best error achieved on DiLiGenT-MV [25] when using ground truth normals is 0.11mm) of best method run on predicted normals and ground truth normals is significantly higher (e.g. 4.2 times vs 1.8), indicating that LUCES-MV is a significantly more challenging benchmark. While all three methods evaluated on DiLiGenT-MV [25] benchmark achieve errors within 0.04mm (ie. 0.2mm, 0.2mm and 0.24mm for NPLMV-PS [31], Supernormal [6] and RNb-NeuS [5]), on LUCES-MV there are clear differences in performance between all three methods. Also at least 6 of 10 of the objects have error larger than 0.3mm indicating that there is plenty of space for improving multi-view photometric stereo methods.

the surfaces are locally correct, the overall shape suffers due to over smoothing of occlusion boundaries. This loss of accuracy (especially compared to LUCES-ST [30]) is explained by the fact that the object distance is more than twice in LUCES-MV than LUCES-ST ($\sim 35\text{cm}$ to $\sim 15\text{cm}$) and thus the reduction of parallax is reducing the value of stereo. DiLiGenT-MV also contains circular motion so the parallax between views is significant.

Multi-view photometric stereo. The worst performing method is the intensity only (I) version of NPLMV-PS [31], which is the only method not utilizing the normal estimates. This signifies that there is significant scope for improvement on the neural rendering for challenging PS objects.

Normal only (N) version of NPLMV-PS [31] is also outperforming the functionally similar Supernormal [6] method on most of the objects with exception of the very smooth ones *Bunny*, *Die* and *Queen*. This signifies that the patch rendering procedure of Supernormal [6] is potentially a loss of accuracy in case of high details (with *House* being an outlier).

Additionally, including N+I on NPLMV-PS [31] significantly improves it compared to its other 2 versions showing that the 2 sources of information act synergistically. Not surprising, the albedo information also allows RNb-NeuS [5] to show very good performance, on most ob-

jects with exception of *Buddha* and *Cup*, yet still being the overall winner with a significant margin (0.55mm mean vs 0.72mm of NPLMV-PS [31]). Nevertheless, this performance is far from the performance observed in DiLiGenT-MV benchmark as per evaluation of [31].

Finally, we provide evaluation of RNb-NeuS [5] (the best overall approach) with ground truth normals as a way to estimate potential performance that could be expected with future improvements on normal estimation methods. Note that this is an imperfect estimate as predicted albedos are also used (as there is no way to compute ground truth albedos) and thus providing relatively mediocre results on the *Cup* (0.51mm mean, 0.27mm median) where the albedo estimation is challenging. Nevertheless, all other objects achieve around 0.05mm to 0.15mm which is considerably better than any actual fair predictions, showing that there is significant scope for future improvements.

6. Conclusion

In this paper, we propose LUCES-MV, the first real-world, multi-view dataset designed for near-field point light source photometric stereo. Our dataset includes 15 objects with diverse materials, each imaged under varying light conditions from an array of 15 LEDs positioned 30 to 40 centimeters from the camera center.

We evaluate state-of-the-art near-field photometric stereo algorithms, highlighting their strengths and limitations across different material and shape complexities. LUCES-MV dataset offers an important benchmark for developing more robust, accurate and scalable real-world Photometric Stereo based 3D reconstruction methods.

References

- [1] A. Agrawal, R. Raskar, and R. Chellappa. What is the range of surface reconstructions from a gradient field? In *European Conference on Computer Vision (ECCV)*, 2006. [2](#)
- [2] N. Alldrin, T. E. Zickler, and D. J. Kriegman. Photometric stereo with non-parametric and spatially-varying reflectance. In *IEEE Conference on Computer Vision and Pattern Recognition (CVPR)*, 2008. [3](#)
- [3] Meta Project Aria. Dataset: Dtc - dense tracking and correspondence dataset. <https://www.projectaria.com/datasets/dtc/>, 2024. Accessed: 2024-11-08. [4](#)
- [4] Mohammed Brahimi, Bjoern Haefner, Zhenzhang Ye, Bastian Goldluecke, and Daniel Cremers. Sparse views near light: A practical paradigm for uncalibrated point-light photometric stereo. In *CVPR*, June 2024. [1, 3, 6](#)
- [5] Baptiste Brument, Robin Bruneau, Yvain Quéau, Jean Mélou, François Lauze, Jean-Denis Durou, and Lilian Calvet. Rnb-neus: Reflectance and normal-based multi-view 3d reconstruction. In *IEEE/CVF Conference on Computer Vision and Pattern Recognition (CVPR)*, 2024. [2, 3, 6, 7, 8, 11, 12, 16, 17](#)
- [6] Xu Cao and Takafumi Taketomi. Supernormal: Neural surface reconstruction via multi-view normal integration. *CVPR*, 2024. [1, 3, 6, 8, 12, 16](#)
- [7] M. K. Chandraker, S. Agarwal, and D. J. Kriegman. Shadowcuts: Photometric stereo with shadows. In *IEEE Conference on Computer Vision and Pattern Recognition (CVPR)*, 2007. [2](#)
- [8] Guanying Chen, Kai Han, Boxin Shi, Yasuyuki Matsushita, and Kwan-Yee K. Wong. Sdps-net: Self-calibrating deep photometric stereo networks. In *CVPR*, 2019. [2](#)
- [9] Guanying Chen, Kai Han, and Kwan-Yee K Wong. Ps-fcn: A flexible learning framework for photometric stereo. In *Proceedings of the European conference on computer vision (ECCV)*, pages 3–18, 2018. [3](#)
- [10] P. Cignoni, M. Callieri, M. Corsini, M. Dellepiane, F. Ganovelli, and G. Ranzuglia. Meshlab: an open-source mesh processing tool. In *Eurographics*, 2008. [4, 6](#)
- [11] Heng Guo, Jiejie Ren, Feishi Wang, Boxin Shi, Mingjun Ren, and Yasuyuki Matsushita. Diligenrt: A photometric stereo dataset with quantified roughness and translucency. In *Proceedings of the IEEE/CVF Conference on Computer Vision and Pattern Recognition (CVPR)*, pages 11810–11820, June 2024. [3](#)
- [12] Heng Guo, Hiroaki Santo, Boxin Shi, and Yasuyuki Matsushita. Edge-preserving near-light photometric stereo with neural surfaces. *arXiv*, 2022. [2](#)
- [13] Clément Hardy, Yvain Quéau, and David Tschumperlé. Msps: A multi-scale network for photometric stereo with a new comprehensive training dataset. *arXiv*, 2023. [2, 5, 6, 16](#)
- [14] S. Ikehata. Cnn-ps: Cnn-based photometric stereo for general non-convex surfaces. In *ECCV*, 2018. [2, 3](#)
- [15] Satoshi Ikehata. Universal photometric stereo network using global lighting contexts. *CVPR*, 2022. [2](#)
- [16] Satoshi Ikehata. Scalable, detailed and mask-free universal photometric stereo. *CVPR*, 2023. [2, 6, 11, 16, 17](#)
- [17] Rasmus Jensen, Anders Dahl, George Vogiatzis, Engin Tola, and Henrik Aanæs. Large scale multi-view stereopsis evaluation. In *CVPR*, pages 406–413, 2014. [4](#)
- [18] Yakun Ju, Cong Zhang, Songsong Huang, Yuan Rao, and Kin-Man Lam. Learning deep photometric stereo network with reflectance priors. In *ICME*, 2023. [2](#)
- [19] Berk Kaya, Suryansh Kumar, Carlos Oliveira, Vittorio Ferrari, and Luc Van Gool. Uncertainty-aware deep multi-view photometric stereo. In *CVPR*, 2022. [3](#)
- [20] Berk Kaya, Suryansh Kumar, Carlos Oliveira, Vittorio Ferrari, and Luc Van Gool. Multi-view photometric stereo revisited. In *WACV*, 2023. [3](#)
- [21] Berk Kaya, Suryansh Kumar, Francesco Sarno, Vittorio Ferrari, and Luc Van Gool. Neural radiance fields approach to deep multi-view photometric stereo. In *WACV*, 2021. [1, 3](#)
- [22] Arno Knapitsch, Jaesik Park, Qian-Yi Zhou, and Vladlen Koltun. Tanks and temples: Benchmarking large-scale scene reconstruction. *ACM Transactions on Graphics (ToG)*, 36(4):1–13, 2017. [4](#)
- [23] Junxuan Li and Hongdong Li. Neural reflectance for shape recovery with shadow handling. In *CVPR*, pages 16221–16230, 2022. [2](#)
- [24] Junxuan Li and Hongdong Li. Self-calibrating photometric stereo by neural inverse rendering. In *ECCV*. Springer, 2022. [2](#)
- [25] Min Li, Zhenglong Zhou, Zhe Wu, Boxin Shi, Changyu Diao, and Ping Tan. Multi-view photometric stereo: A robust solution and benchmark dataset for spatially varying isotropic materials. *IEEE Trans. Image Process.*, 2020. [1, 2, 3, 6, 8, 11](#)
- [26] Ruilong Li, Hang Gao, Matthew Tancik, and Angjoo Kanazawa. Nerfacc: Efficient sampling accelerates nerfs. *arXiv*, 2023. [12](#)
- [27] Zhaoshuo Li, Thomas Müller, Alex Evans, Russell H Taylor, Mathias Unberath, Ming-Yu Liu, and Chen-Hsuan Lin. Neuralangelo: High-fidelity neural surface reconstruction. In *IEEE Conference on Computer Vision and Pattern Recognition (CVPR)*, 2023. [2, 3, 11, 12, 16, 18](#)
- [28] Chen-Hsuan Lin, Wei-Chiu Ma, Antonio Torralba, and Simon Lucey. Barf: Bundle-adjusting neural radiance fields. In *Proceedings of the IEEE/CVF International Conference on Computer Vision (ICCV)*, pages 5741–5751, October 2021. [5](#)
- [29] Yuan Liu, Peng Wang, Cheng Lin, Xiaoxiao Long, Jiepeng Wang, Lingjie Liu, Taku Komura, and Wenping Wang. Nero: Neural geometry and brdf reconstruction of reflective objects from multiview images. In *SIGGRAPH*, 2023. [1, 3](#)
- [30] Fotios Logothetis, Ignas Budvytis, and Roberto Cipolla. A neural height-map approach for the binocular photometric stereo problem. *WACV*, 2024. [1, 3, 4, 6, 8, 11, 12, 16, 17](#)

- [31] Fotios Logothetis, Ignas Budvytis, and Roberto Cipolla. Nplmv-ps: Neural point-light multi-view photometric stereo. In *WACV*, 2025. [1](#), [2](#), [3](#), [6](#), [8](#), [12](#), [16](#)
- [32] Fotios Logothetis, Ignas Budvytis, Roberto Mecca, and Roberto Cipolla. PX-NET: Simple, Efficient Pixel-Wise Training of Photometric Stereo Networks. In *ICCV*, 2021. [2](#), [6](#)
- [33] Fotios Logothetis, Roberto Mecca, Ignas Budvytis, and Roberto Cipolla. A cnn based approach for the point-light photometric stereo problem. *IJCV*, 2022. [2](#), [6](#), [11](#), [16](#)
- [34] Fotios Logothetis, Roberto Mecca, and Roberto Cipolla. Semi-calibrated near field photometric stereo. In *CVPR*, 2017. [3](#)
- [35] Fotios Logothetis, Roberto Mecca, and Roberto Cipolla. A differential volumetric approach to multi-view photometric stereo. In *ICCV*, 2019. [3](#)
- [36] R. Mecca and M. Falcone. Uniqueness and approximation of a photometric shape-from-shading model. *SIAM J. Imag. Sci.*, 6(1):616–659, 2013. [2](#)
- [37] Roberto Mecca, Fotios Logothetis, Ignas Budvytis, and Roberto Cipolla. Lucas: A dataset for near-field point light source photometric stereo. In *BMVC*, 2021. [1](#), [4](#), [11](#)
- [38] R. Mecca, Y. Quéau, F. Logothetis, and R. Cipolla. A single lobe photometric stereo approach for heterogeneous material. *SIAM Journal on Imaging Sciences*, 2016. [3](#)
- [39] Roberto Mecca, A. Wetzler, A. Bruckstein, and R. Kimmel. Near Field Photometric Stereo with Point Light Sources. *SIAM Journal on Imaging Sciences*, 2014. [4](#), [11](#)
- [40] Ben Mildenhall, Pratul P. Srinivasan, Matthew Tancik, Jonathan T. Barron, Ravi Ramamoorthi, and Ren Ng. Nerf: Representing scenes as neural radiance fields for view synthesis. In *ECCV*, 2020. [1](#), [3](#)
- [41] Thomas Müller. tiny-cuda-nn, 4 2021. [12](#)
- [42] Matthias Nießner, Michael Zollhöfer, Shahram Izadi, and Marc Stamminger. Real-time 3d reconstruction at scale using voxel hashing. *ACM Trans. Graph.*, 2013. [3](#)
- [43] Jaesik Park, Sudipta N. Sinha, Yasuyuki Matsushita, Yu-Wing Tai, and In So Kweon. Robust multiview photometric stereo using planar mesh parameterization. *IEEE Transactions on Pattern Analysis and Machine Intelligence*, 39(8):1591–1604, 2017. [3](#)
- [44] Jeong Joon Park, Peter Florence, Julian Straub, Richard Newcombe, and Steven Lovegrove. Deepsdf: Learning continuous signed distance functions for shape representation. In *CVPR*, 2019. [1](#)
- [45] Y. Quéau, B. Durix, Tao Wu, D. Cremers, F. Lauze, and J.-D. Durou. Led-based photometric stereo: Modeling, calibration and numerical solution. *JMIV*, 2018. [4](#)
- [46] Y. Quéau and J.-D. Durou. Edge-preserving integration of a normal field: Weighted least squares, TV and L1 approaches. In *SSVM*, 2015. [3](#)
- [47] Jieji Ren, Feishi Wang, Jiahao Zhang, Qian Zheng, Mingjun Ren, and Boxin Shi. Diligent102: A photometric stereo benchmark dataset with controlled shape and material variation. In *Proceedings of the IEEE/CVF Conference on Computer Vision and Pattern Recognition (CVPR)*, pages 12581–12590, June 2022. [3](#)
- [48] Hiroaki Santo, Masaki Samejima, Yusuke Sugano, Boxin Shi, and Yasuyuki Matsushita. Deep photometric stereo network. In *Proceedings of the IEEE international conference on computer vision workshops*, pages 501–509, 2017. [2](#), [3](#)
- [49] Johannes Lutz Schönberger and Jan-Michael Frahm. Structure-from-motion revisited. In *CVPR*, 2016. [5](#)
- [50] Boxin Shi, Zhe Wu, Zhipeng Mo, Dinglong Duan, Sai-Kit Yeung, and Ping Tan. A benchmark dataset and evaluation for non-lambertian and uncalibrated photometric stereo. In *Proceedings of the IEEE Conference on Computer Vision and Pattern Recognition (CVPR)*, June 2016. [3](#), [4](#), [6](#)
- [51] Dor Verbin, Peter Hedman, Ben Mildenhall, Todd Zickler, Jonathan T. Barron, and Pratul P. Srinivasan. Ref-nerf: Structured view-dependent appearance for neural radiance fields. *CVPR*, 2022. [1](#), [3](#)
- [52] G. Vogiatzis and C. Hernández. Practical 3d reconstruction based on photometric stereo. In *Computer Vision: Detection, Recognition and Reconstruction*. Springer, 2010.
- [53] Feishi Wang, Jieji Ren, Heng Guo, Mingjun Ren, and Boxin Shi. Diligent-pi: Photometric stereo for planar surfaces with rich details-benchmark dataset and beyond. In *Proceedings of the IEEE/CVF International Conference on Computer Vision*, pages 9477–9487, 2023. [3](#)
- [54] Peng Wang, Lingjie Liu, Yuan Liu, Christian Theobalt, Taku Komura, and Wenping Wang. Neus: Learning neural implicit surfaces by volume rendering for multi-view reconstruction. *NeurIPS*, 2021. [3](#)
- [55] L. B. Wolff and E. Angelopoulou. 3-D stereo using photometric ratios. In *European Conference on Computer Vision (ECCV)*, pages 247–258, 1994. [2](#)
- [56] Ying Xiong, Ayan Chakrabarti, Ronen Basri, Steven J Gortler, David W Jacobs, and Todd Zickler. From shading to local shape. *IEEE transactions on pattern analysis and machine intelligence*, 37(1):67–79, 2014. [3](#)
- [57] Wenqi Yang, Guanying Chen, Chaofeng Chen, Zhenfang Chen, and Kwan-Yee K. Wong. Ps-nerf: Neural inverse rendering for multi-view photometric stereo. In *ECCV*, 2022. [1](#), [3](#)
- [58] Wenqi Yang, Guanying Chen, Chaofeng Chen, Zhenfang Chen, and Kwan-Yee K. Wong. S3-NeRF: Neural reflectance field from shading and shadow under a single viewpoint. In Alice H. Oh, Alekh Agarwal, Danielle Belgrave, and Kyunghyun Cho, editors, *NeurIPS*, 2022. [2](#)
- [59] Lior Yariv, Jiatao Gu, Yoni Kasten, and Yaron Lipman. Volume rendering of neural implicit surfaces. In *Thirty-Fifth Conference on Neural Information Processing Systems*, 2021. [3](#)
- [60] Lior Yariv, Yoni Kasten, Dror Moran, Meirav Galun, Matan Atzmon, Basri Ronen, and Yaron Lipman. Multiview neural surface reconstruction by disentangling geometry and appearance. *Advances in Neural Information Processing Systems*, 33:2492–2502, 2020. [3](#)
- [61] Jingyang Zhang, Yao Yao, Shiwei Li, Jingbo Liu, Tian Fang, David McKinnon, Yanghai Tsin, and Long Quan. Neif++: Inter-reflectable light fields for geometry and material estimation. In *International Conference on Computer Vision (ICCV)*, 2023. [1](#), [3](#)

- [62] Dongxu Zhao, Daniel Lichy, Pierre-Nicolas Perrin, Jan-Michael Frahm, and Soumyadip Sengupta. Mvpsnet: Fast generalizable multi-view photometric stereo. In *Proceedings of the IEEE/CVF International Conference on Computer Vision (ICCV)*, pages 12525–12536, October 2023. 3
- [63] Michael Zollhöfer, Angela Dai, Matthias Innmann, Chenglei Wu, Marc Stamminger, Christian Theobalt, and Matthias Nießner. Shading-based refinement on volumetric signed distance functions. *ACM Trans. Graph.*, 2015. 3

A. Additional Dataset Details

In this section we provide additional details of LUCES-MV dataset which were omitted from the main paper. In particular, we discuss the unposed objects, and images used for camera intrinsic calibration and light calibration.

A.1. Ground truth meshes for the objects

Figure 6 shows the ground truth meshes of the unposed objects namely *Ball*, *Bell*, *Glass*, *Jar*, *Tool*. Preview images (average photometric stereo image) for all objects in all views are shown in Figures 7 8 and 9. For all objects, the stereo pair views are grouped vertically for a total of 6 views (every 60°). The approximate real world dimensions of all objects are shown in Table 3.

A.2. Intrinsic calibration images

Intrinsic parameter calibration was performed using a the standard OpenCV calibration toolbox and a 10×9 calibration pattern from <https://calib.io/>. 420 images are captured to ensure orientation, location and scale variation as shown in Figure 10. These images will be made available as a part of files representing the dataset.

A.3. Light calibration images

Light calibration was performed using the same point-wise differentiable renderer from the original LUCES [37] dataset. In sort, the flat object is approximate Lambertian, with albedo 0.99 (according to manufactured specifications) with no shadows and interefection, thus following irradiance Equation 2 of main text. 390 images (2 cameras, 15 lights, 13 view-points) are captured to ensure orientation and scale variation as shown in Figure 10. These images will be made available as a part of files representing the dataset. We hope that these calibration images will encourage future research into neural light attenuation models/point light radiance fields, that should be more accurate than the SOTA analytic calibrated LED model of [39].

B. Additional results

The section contains additional results not reported in the main paper. In particular, it provides a discussion on why certain objects used in LUCES-MV are significantly

more challenging than objects used in DiLiGenT-MV [25]. It also visualises results of binocular photometric stereo results of [30], provides predicted albedo image visualisations of UniPS [16] (used by RNb-NeuS [5]), lists running times of competing multi-view photometric stereo methods and shows additional results of non-PS reconstruction method, Neuroangelo [27].

B.1. Object choices

The objects in LUCES-MV were chosen to have a varied selection of shapes and materials. *Ball* is made of sponge which is missing in competing datasets. *Bowl* has an extreme concavity and a specular material hence experiencing challenging shadows and interreflections. *Buddha* is made of marble which is mostly diffuse but contains high frequency details that are also highly specular. *Bell* and *Cup* are metallic with *Cup* being much shinier (and thus harder) than *Bell*. *Bunny* and *Hippo* are made of shiny plastic but are contrasted as *Bunny* is more textured than *Hippo*. Indeed, having multiple object of similar material can be help disentangle the effect of geometry vs material on the difficulty. Thus the painted wood *Die* as well as the wooden *Tool* and top of the *Jar* are aimed to compare different wood configurations. The *House* has very complicated geometry but high amount of texture. The *Squirrel* is shiny porcelain (the main body of the *Jar* is also porcelain) with a lot of self reflection in the bottom part. Plaster objects *Owl* and *Queen* are fairly diffuse and thus are aimed to be relatively easy; however, cast shadows at concave regions did pose some challenge to current SOTA methods.

Finally, we also include the semi-transparent *Glass* which is currently unsolvable for most PS and neural reconstruction methods to encourage future research in that directions.

B.2. Binocular photometric stereo

Quantitative visualization of the results of the binocular photometric stere method [30] is shown in Figure 11. It is noted that the recovered shape exhibits significant bending and smoothing of the occlusion boundaries, similar to monocular PS (i.e. [33]), and that explains the relatively low quantitative performance. Thus, for applications requiring fast data capture (e.g. grasping point estimation for robotics), additional future research is required to achieve sub-millimeter precision.

B.3. Albedo images from Uni-PS [16]

Figure 12 shows albedo images estimated by Uni-PS [16]. These images are used by the SOTA multi-view PS method RNb-NeuS [5]. These albedo predictions look reasonable (since there is no easy way to obtain ground truth albedos, the can only be evaluated qualitatively) with notable exceptions the metallic *Cup* and the black numbers on

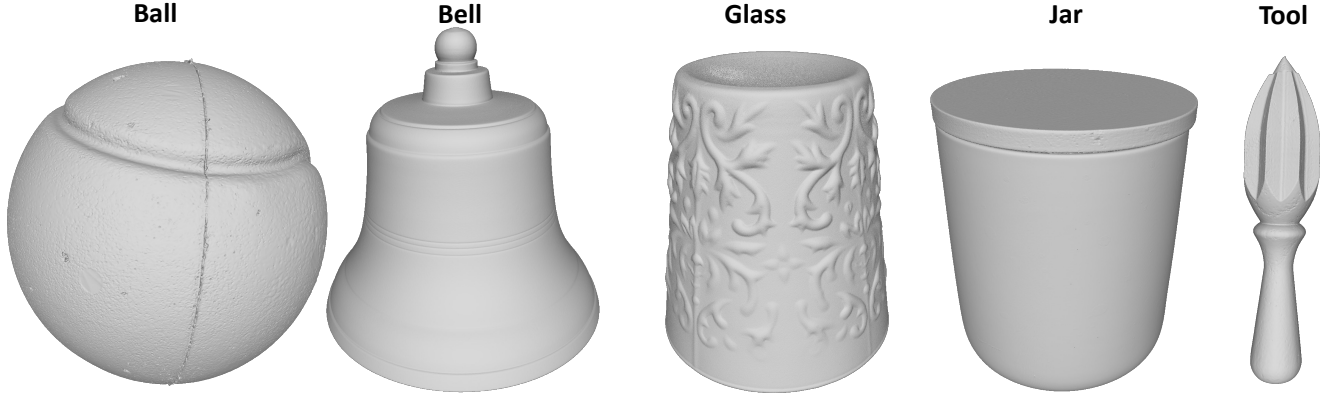


Figure 6. Ground truth meshes for the additional, *unposed* objects namely *Ball*, *Bell*, *Glass*, *Jar*, *Tool*. The respective average photometric stereo images are shown in Figure 9.

Object	Bowl	Buddha	Bunny	Cup	Die
Dimensions (mm)	50×30×70	85×200×170	50×85×90	60×70×70	65×65×65
Object	Hippo	House	Owl	Queen	Squirrel
Dimensions (mm)	40×50×95	105×80×70	65×45×80	60×60×135	50×70×115
Object	Ball	Bell	Glass	Jar	Tool
Dimensions (mm)	70×70×70	105×105×110	90×90×100	100×100×115	30×30×140

Table 3. This table provides approximate dimensions of the objects used in LUCES-MV. Note that precise sizes of objects can be computed directly from the ground truth meshes provided.

the *Die*. Additionally, concavities on *Buddha* and *Queen* appear darker than the surrounding object, however in reality the real objects should be more uniform.

B.4. Running times

Table 4 shows approximate running times and GPU memory usage for all methods. Note that RNb-NeuS [5], Supernormal [6] and Neuroangelo [27] (using ‘instant’ version, see Section B.5) are using direct GPU acceleration³ and thus are significantly faster than Binocular [30] and NPLMV-PS [31] which have pure tensorflow implementations. Additionally, the rendering mode of NPLMV-PS [31] significantly increases the computational cost as well. Note that all methods were run with the default settings and no effort to optimize their computational time and GPU memory usage.

B.5. Additional results of Neuroangelo [27]

Figure 13 shows additional results (on objects *Bowl*, *Buddha*, *House*) of non-PS reconstruction method, Neuroangelo [27]. Note, that to perform reconstruction, average PS images from all 36×2 viewpoints and poses and sparse

³Using CUDNN [41] NERFACC [26] and other speed-up techniques. Additionally, RNb-NeuS [5] has a full CUDA version.

point cloud estimated by SFM library Colmap were used. For other objects pose estimation failed. This is not meant to be a fair comparison with the PS competitors (that use less views, more images per view, segmentation masks but not sparse point cloud) but rather a demonstration that non-PS reconstruction methods, despite their high re-rendering quality, their estimated shape is clearly worse than one estimated by multi-view photometric stereo methods.

It should be noted though that we used the fast version from <https://github.com/hugoycj/Instant-angelo/> which may be potentially worse than the original one with several orders of magnitude of computational speed-up.

C. Limitations

Since this is a dataset paper the limitations are mainly to do with the size of the dataset. Ideally, it would be scaled to 100s and 1000s of objects as a future work. It also has materials which are generally smooth and do not contain micro structures (e.g. fabrics). While the methods evaluated are SOTA for their respective tasks, we hope that this dataset will be used to evaluate more of the past and future works.

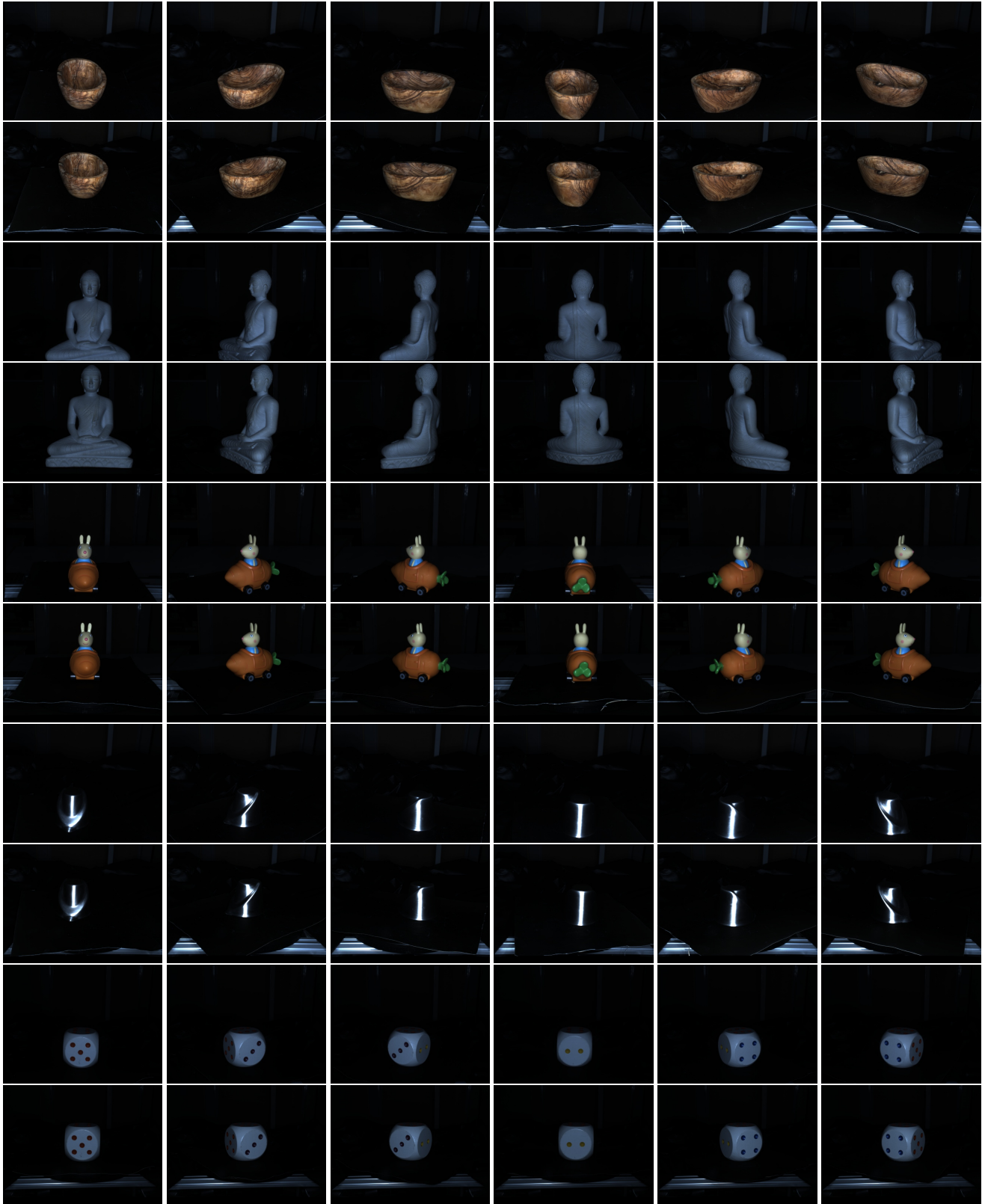


Figure 7. Average PS image for all views for *Bowl*, *Buddha*, *Bunny*, *Cup*, *Dice*.



Figure 8. Average PS image for all views for *Hippo*, *House*, *Owl*, *Queen*, *Squirrel*.

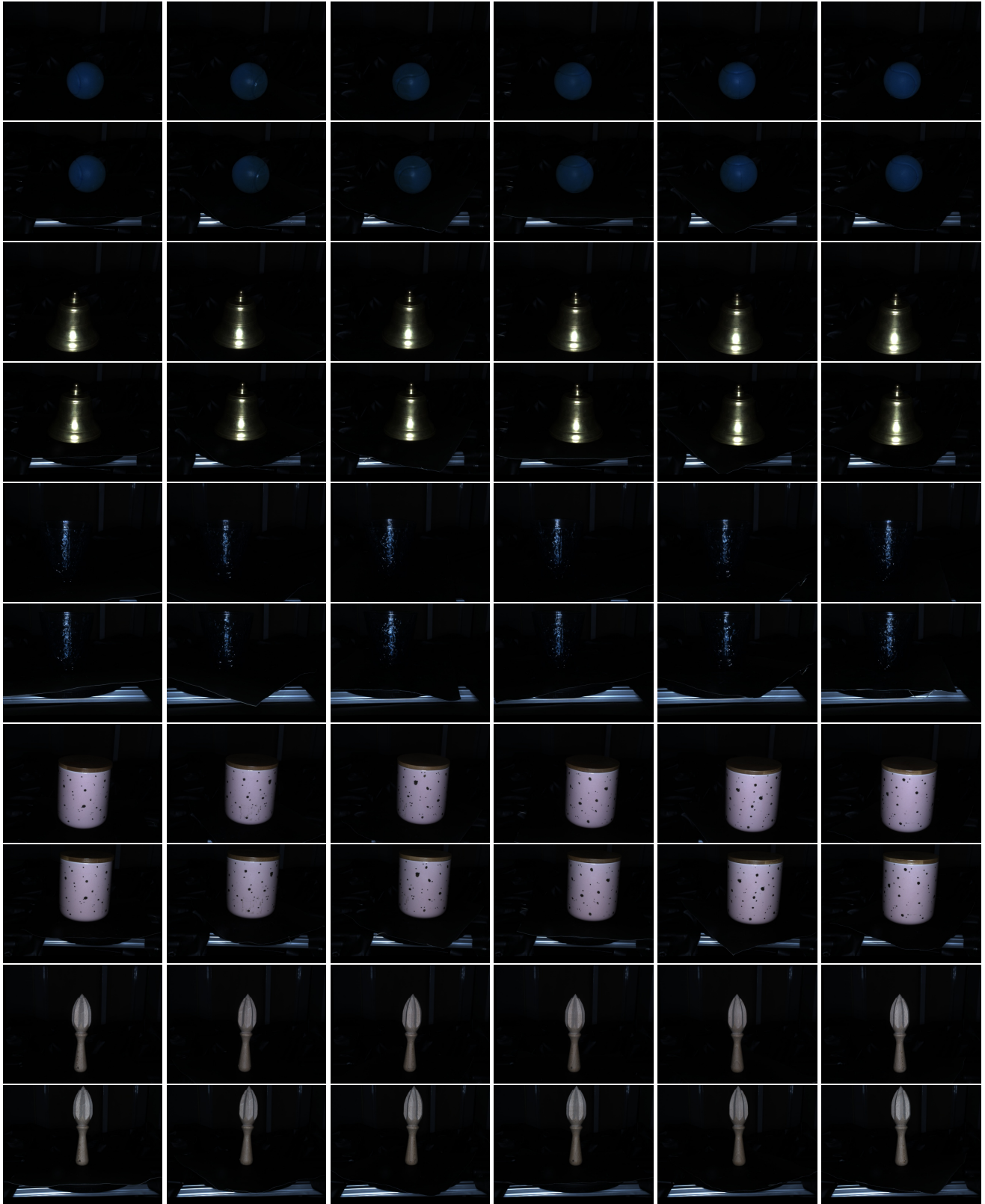


Figure 9. Average PS image for all views for *Ball*, *Bell*, *Glass*, *Jar*, *Tool*.

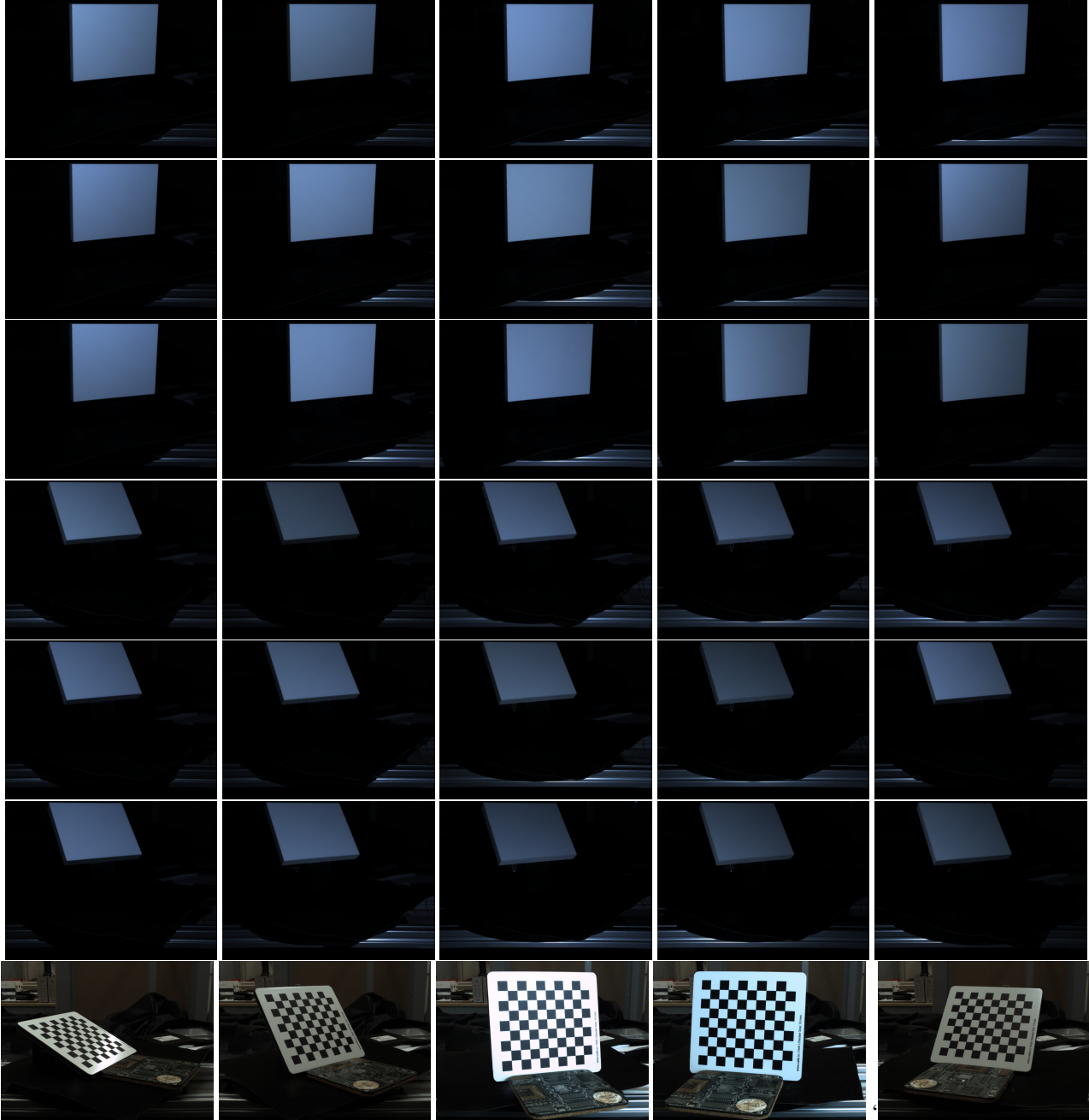


Figure 10. This figure shows all 15 images from 2 out of the 26 views used for calibration. It also shows 5 of 420 checkerboard images. Note that to maximize the image quality of the checkerboard images, additional external illumination was used.

Method	UniPS [16]	Uni MS-PS [13]	NF-PX-Net [33]	Binocular [30]	Neuralangelo [27]	RNb-NeuS [5]	Supernormal [6]	NPLMV-PS(N) [31]	NPLMV-PS [31] (N+I)
Time	2m	20m	5m	5h	40m	5m	5m	3h	8h
Memory	20GB	3GB	1GB	10GB	10GB	15GB	5GB	10GB	25GB

Table 4. Approximate running times and GPU memory usage on single NVIDIA RTX A6000. Note that single view methods UniPS [16], Uni MS-PS [13] and NF-PX-Net [33] are reported per single view and are significantly varied depending on the number of foreground pixels; the reported numbers are an approximate overall average.

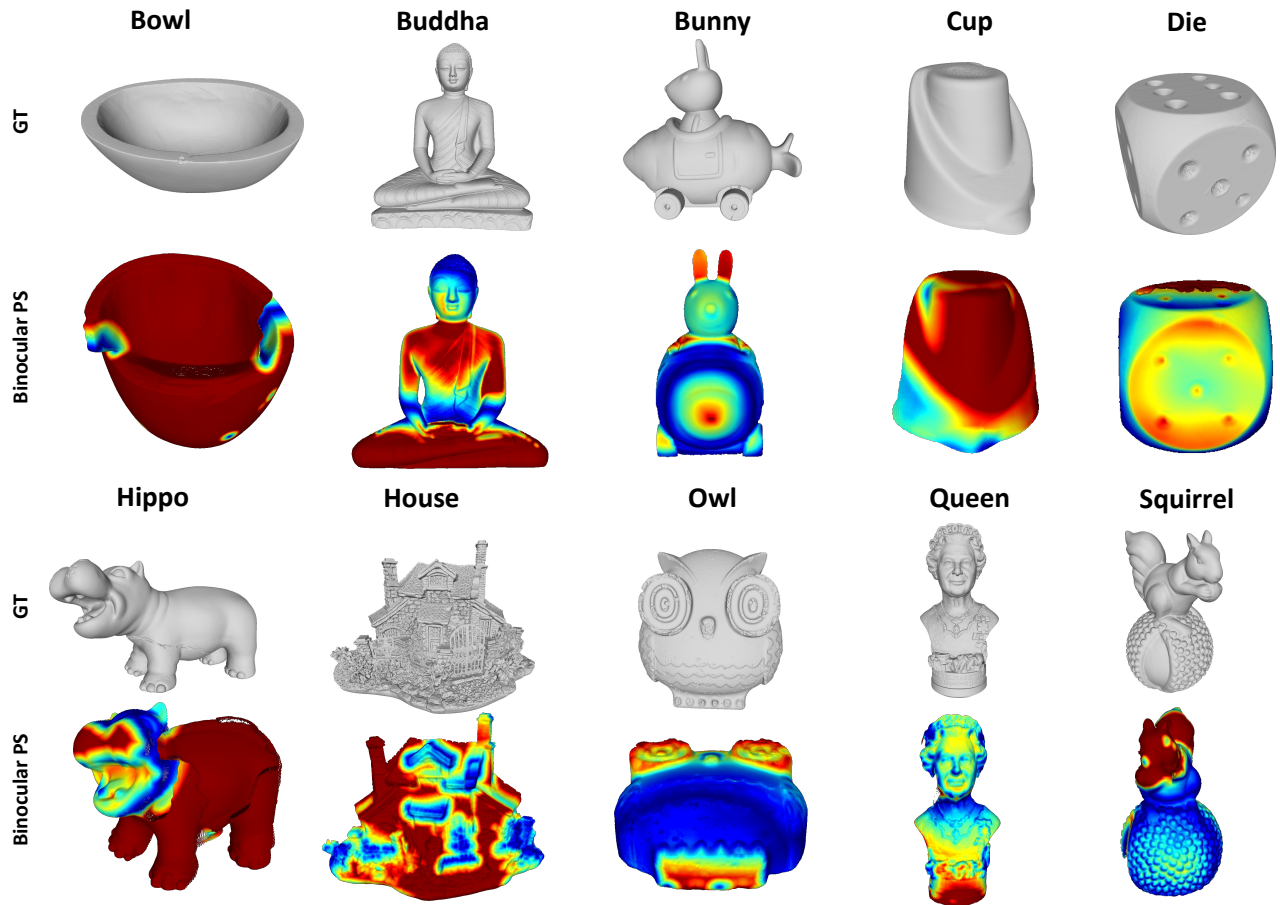


Figure 11. This figure shows results of binocular photometric stereo of [30]. First row shows the ground truth shape and the second row shows the shape error. Unlike in the similar figure in the main paper here red color corresponds to a 5mm error (not 1mm).

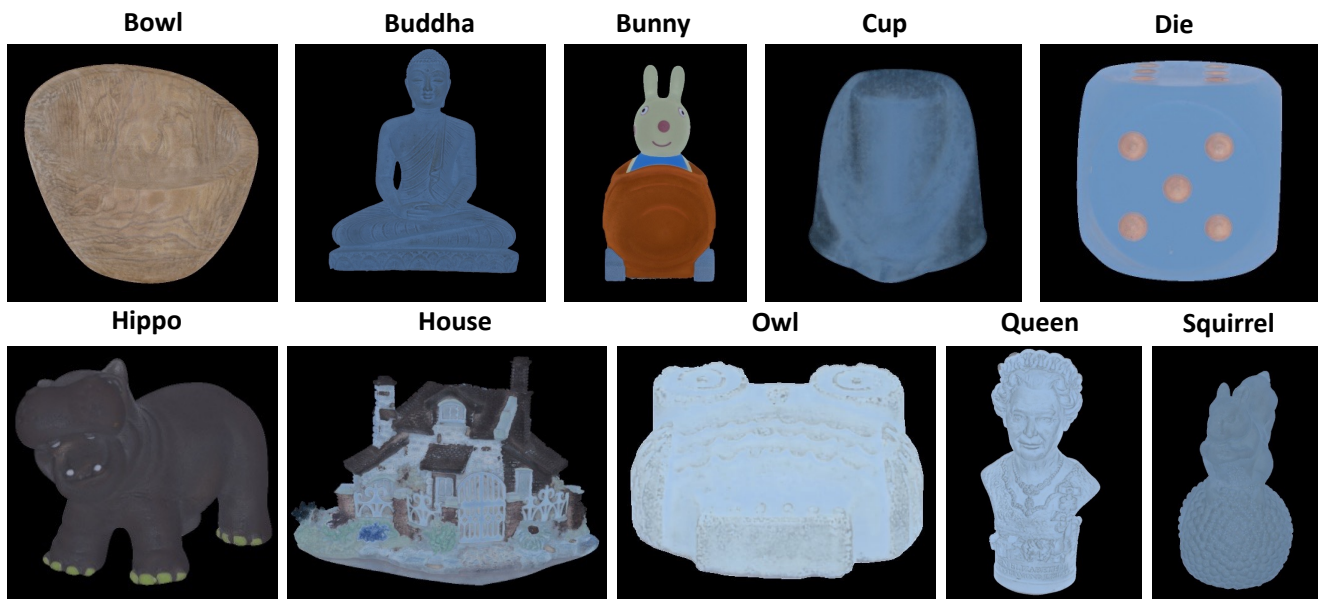


Figure 12. Albedo predictions from UniPS [16], used by RNb-NeuS [5].

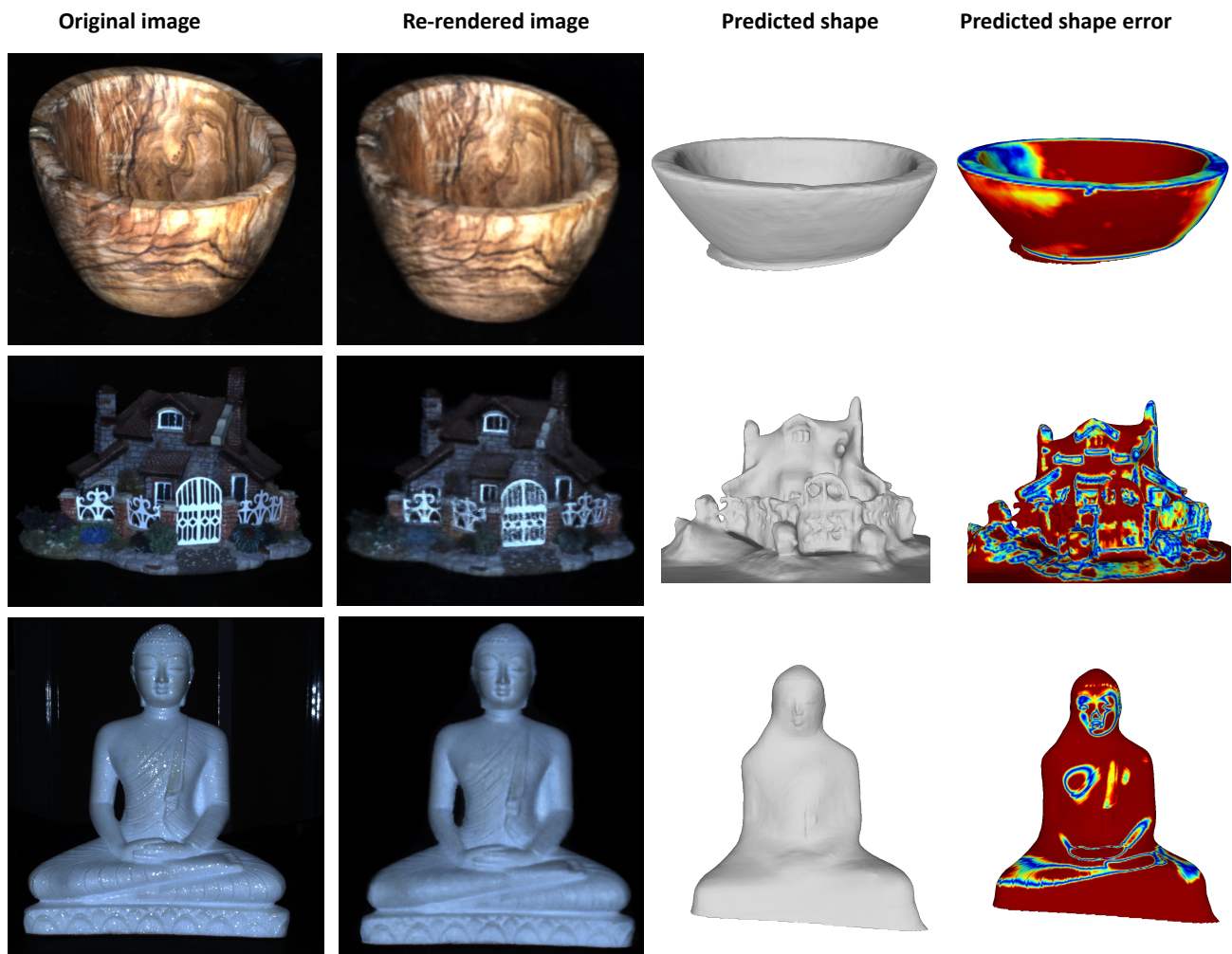


Figure 13. Additional results of classical (non-PS) NeRF method of Neuralangelo [27]. Red color corresponds to a 1mm error.